Three-dimensional STED microscopy of aberrating tissue using dual adaptive optics

Brian R. Patton,[1] Daniel Burke,[1] David Owald,[1] Travis J. Gould,[2,3] Joerg Bewersdorf,[2,4] and Martin J. Booth[1,5,*]

[1] *Centre for Neural Circuits and Behaviour, University of Oxford, Mansfield Road, Oxford OX1 3SR, UK*

[2] *Department of Cell Biology, Yale University School of Medicine, New Haven, Connecticut 06511, USA*

[3] *Department of Physics and Astronomy, Bates College, Lewiston, Maine 04240, USA*

[4] *Department of Biomedical Engineering, Yale University, New Haven, Connecticut 06511, USA*

[5] *Department of Engineering Science, University of Oxford, Parks Rd., Oxford OX1 3PJ, UK*

[*] *martin.booth@eng.ox.ac.uk*

Abstract: When imaging through tissue, the optical inhomogeneities of the sample generate aberrations that can prevent effective Stimulated Emission Depletion (STED) imaging. This is particularly problematic for 3D-enhanced STED. We present here an adaptive optics implementation that incorporates two adaptive optic elements to enable correction in all beam paths, allowing performance improvement in thick tissue samples. We use this to demonstrate 3D STED imaging of complex structures in *Drosophila melanogaster* brains.

OCIS codes: (100.6640) Superresolution;(110.1080) Active or adaptive optics; (170.5810) Scanning microscopy; (170.6930) Tissue.

References and links

1. N. Urban, K. Willig, S. Hell, and U. Naegerl, "STED nanoscopy of actin dynamics in synapses deep inside living brain slices," Biophys. J. **101**, 1277 – 1284 (2011).
2. G. Lukinavicius, L. Reymond, E. D'Este, A. Masharina, F. Gottfert, H. Ta, A. Guther, M. Fournier, S. Rizzo, H. Waldmann, C. Blaukopf, C. Sommer, D. W. Gerlich, H.-D. Arndt, S. W. Hell, and K. Johnsson, "Fluorogenic probes for live-cell imaging of the cytoskeleton," Nat. Meth. **11**, 731–733 (2014).
3. F. Goettfert, C. A. Wurm, V. Mueller, S. Berning, V. C. Cordes, A. Honigmann, and S. W. Hell, "Coaligned dual-channel STED nanoscopy and molecular diffusion analysis at 20 nm resolution," Biophys. J. **105**, L01–L03 (2013).
4. D. Wildanger, B. R. Patton, H. Schill, L. Marseglia, J. P. Hadden, S. Knauer, A. Schoenle, J. G. Rarity, J. L. O'Brien, S. W. Hell, and J. M. Smith, "Solid immersion facilitates fluorescence microscopy with nanometer resolution and sub-angstrom emitter localization," Adv. Mater. **24**, OP309–OP313 (2012).
5. J. Arlt and M. J. Padgett, "Generation of a beam with a dark focus surrounded by regions of higher intensity:the optical bottle beam," Opt. Lett. **25**, 191–193 (2000).
6. J. A. Kubby, ed., *Adaptive Optics for Biological Imaging* (CRC, 2013).
7. M. J. Booth, "Adaptive optical microscopy: the ongoing quest for a perfect image," Light Sci. Appl. **3**, 165– (2014).
8. M. Booth, D. Andrade, D. Burke, B. Patton, and M. Zurauskas, "Aberrations and adaptive optics in super-resolution microscopy," Microscopy **64**(4), 251-261 (2015).
9. T. J. Gould, D. Burke, J. Bewersdorf, and M. J. Booth, "Adaptive optics enables 3D STED microscopy in aberrating specimens," Opt. Express **20**, 20998–21009 (2012).

#259364 Received 12 Feb 2016; revised 23 Mar 2016; accepted 26 Mar 2016; published 13 Apr 2016

10. B. R. Patton, D. Burke, R. Vrees, and M. J. Booth, "Is phase-mask alignment aberrating your STED microscope?" Meth. Appl. Fluoresc. **3**, 024002 (2015).
11. S. Deng, L. Liu, Y. Cheng, R. Li, and Z. Xu, "Effects of primary aberrations on the fluorescence depletion patterns of STED microscopy," Opt. Express **18**, 1657–1666 (2010).
12. M. Booth, M. Neil, and T. Wilson, "Aberration correction for confocal imaging in refractive-index-mismatched media," J. Microsc. **192**, 90–98 (1998).
13. A. Jesacher and M. J. Booth, "Parallel direct laser writing in three dimensions with spatially dependent aberration correction," Opt. Express **18**, 21090–21099 (2010).
14. G. Donnert, J. Keller, R. Medda, M. A. Andrei, S. O. Rizzoli, R. Lhrmann, R. Jahn, C. Eggeling, and S. W. Hell, "Macromolecular-scale resolution in biological fluorescence microscopy," Proc. Nat. Acad. Sci. U.S.A. **103**, 11440–11445 (2006).
15. E. Auksorius, B. R. Boruah, C. Dunsby, P. M. P. Lanigan, G. Kennedy, M. A. A. Neil, and P. M. W. French, "Stimulated emission depletion microscopy with a supercontinuum source and fluorescence lifetime imaging," Opt. Lett. **33**, 113–115 (2008).
16. T. J. Gould, E. B. Kromann, D. Burke, M. J. Booth, and J. Bewersdorf, "Auto-aligning stimulated emission depletion microscope using adaptive optics," Opt. Lett. **38**, 1860–1862 (2013).
17. M. A. A. Neil, M. J. Booth, and T. Wilson, "New modal wave-front sensor: a theoretical analysis," J. Opt. Soc. Am. A **17**, 1098–1107 (2000).
18. A. Thayil and M. Booth, "Self calibration of sensorless adaptive optical microscopes," J. Euro. Opt. Soc. Rapid Publ. **6**, 11045 (2011).
19. W. Saxton and W. Baumeister, "The correlation averaging of a regularly arranged bacterial cell envelope protein," J. Microsc. **127**, 127–138 (1982).
20. N. Banterle, K. H. Bui, E. A. Lemke, and M. Beck, "Fourier ring correlation as a resolution criterion for super-resolution microscopy," J. Struct. Biol. **183**, 363–367 (2013).
21. R. P. J. Nieuwenhuizen, K. A. Lidke, M. Bates, D. L. Puig, D. Grunwald, S. Stallinga, and B. Rieger, "Measuring image resolution in optical nanoscopy," Nat. Meth. **10**, 557–562 (2013).
22. M. van Heel and M. Schatz, "Fourier shell correlation threshold criteria," J. Struct. Biol. **151**, 250–262 (2005).
23. A. Facomprez, E. Beaurepaire, and D. Débarre, "Accuracy of correction in modal sensorless adaptive optics," Opt. Express **20**, 2598–2612 (2012).
24. S. Galiani, B. Harke, G. Vicidomini, G. Lignani, F. Benfenati, A. Diaspro, and P. Bianchini, "Strategies to maximize the performance of a STED microscope," Opt. Express **20**, 7362–7374 (2012).
25. A. Mahr and H. Aberle, "The expression pattern of the drosophila vesicular glutamate transporter: A marker protein for motoneurons and glutamatergic centers in the brain," Gene Expression Patterns **6**, 299 – 309 (2006).
26. D. Owald, J. Felsenberg, C. Talbot, G. Das, E. Perisse, W. Huetteroth, and S. Waddell, "Activity of defined mushroom body output neurons underlies learned olfactory behavior in drosophila," Neuron **86**, 417 – 427 (2015).
27. R. W. Daniels, C. A. Collins, K. Chen, M. V. Gelfand, D. E. Featherstone, and A. DiAntonio, "A single vesicular glutamate transporter is sufficient to fill a synaptic vesicle," Neuron **49**, 11–16 (2006).
28. D. A. Green, "A colour scheme for the display of astronomical intensity images," Bull. Astronom. Soc. India **39**, 289–295 (2011).
29. S. Berning, K. I. Willig, H. Steffens, P. Dibaj, and S. W. Hell, "Nanoscopy in a living mouse brain," Science **335**, 551 (2012).

1. Introduction

Far-field super-resolution fluorescence microscopy is transforming biological science by permitting the observation of structures and processes that were inaccessible using microscopes operating at conventional resolutions [1, 2]. One such method, stimulated emission depletion (STED) microscopy, has facilitated imaging at resolutions down to 20 nm in living cells [3] and 2.4 nm when imaging defects in diamond [4]. The STED method relies upon the use of a depletion beam that consists of a high focal intensity ring surrounding a region of minimum, ideally zero, intensity. This ensures that excited molecules are depleted in the high intensity ring, but not at the centre of the depletion beam, resulting in confinement of the remaining excited molecules to a region much smaller than the original excitation spot. The most common implementation of STED microscopy provides two-dimensional (2D) resolution enhancement using a depletion beam generated by a helicoidal phase plate in a conjugate pupil plane of the objective. Three-dimensional (3D) resolution enhancement can be implemented using a different phase plate that creates a so-called "bottle beam" in which a zero intensity point is surrounded in all directions by higher intensity [5]. This latter configuration offers better 3D imaging ability

#259364 Received 12 Feb 2016; revised 23 Mar 2016; accepted 26 Mar 2016; published 13 Apr 2016

but is more difficult to implement in practice. The 3D STED configuration is more sensitive to aberrations than the 2D STED implementation, which is particularly problematic when imaging deep inside specimens. These aberrations, which are often introduced by refractive index variations within specimens, can be corrected using adaptive optics [6–8]. AO techniques have been demonstrated previously in STED microscopes using liquid crystal spatial light modulators (SLMs) to correct the aberrations of the more critical depletion beam [9, 10]. However, the STED microscope consists of three beam paths: the excitation path, the depletion path, and the emission path – all of which are affected by aberrations. It is clear that full aberration correction in the STED microscope requires compensation of specimen-induced aberrations in all three of these paths and, due to the polarization dependence of the SLM it was not possible to correct all three beam paths with SLM only techniques. We demonstrate such an AO that permits effective 3D STED imaging of biological structures in tissue specimens. This development represents an essential step in enabling super-resolution imaging at greater depth.

2. Design of dual AO 3D STED system

All three of the beam paths in a STED microscope pass through the same specimen refractive index structure that gives rise to the aberrations. If dispersion in the specimen is negligible (this is usually a reasonable assumption in biological specimens), then the optical path length will be the same for the different wavelengths of light that pass through the three paths (although the phase aberrations will be different). Simultaneous correction of these aberrations is therefore best implemented using a deformable mirror (DM) placed in the common beam path. The change in the position of the DM surface corresponds directly to a change in optical path length and hence the correct phase correction is generated at each wavelength. Even though the DM compensates aberrations, it is still desirable to use a SLM in the depletion beam path in order to implement the beam-shaping phase masks. This is important as the shapes produced by the DM are limited by its actuator structure, whereas the SLM can produce more complex phase distributions and the STED phase masks are required only in the depletion beam. Finally, the SLM can perform fine correction of residual aberrations that might not be removed by the DM – we demonstrate in this paper that this is useful, as the structured focus of the depletion beam shows more sensitivity to aberrations than the excitation focus.

We have modeled the STED imaging process in the presence of a typical specimen aberration component, following the procedure in [11], in order to demonstrate why a DM is necessary for deep tissue imaging. We show the effects of spherical aberration from a refractive index mismatch for a 1.4 NA oil immersion lens (n=1.5) focussing 15 μm into a glycerol-based medium (n=1.44) using a depletion wavelength of 760 nm and an excitation and emission wavelength of 635 nm. The excitation and peak emission wavelengths for the dyes used differ by only 30 nm; we set them as equal to reduce computational complexity. The magnitudes of the effects we demonstrate greatly exceed any minor changes this wavelength equality will introduce. The high NA defocus component was removed by minimisation of phase variance [12, 13]. In all cases we calculated the PSF at the nominal focussing depth; this was to allow observation of any shift of the maximum in intensity. Increasing z corresponds to increasing depth in the sample. Figures 1(a) and 1(b) show xz slices incorporating the superposition of the confocal PSF with the depletion PSF for the 2D and 3D STED modes for both fully aberrated (i.e. with no correction) and with correction only in the depletion beam. The focal depth was 15 μm. The saturation factor for both STED modes was set to 10 – this value results in an unaberrated 2D STED resolution of 125 nm, a factor of 2.3 better than the diffraction limited resolution observed in the confocal case. For the 3D STED mode, the dominant resolution increase is in the axial direction and a saturation factor of 10 results in an unaberrated z-resolution of 291 nm, a factor of 2.2 increase over the confocal axial resolution. Maximum intensities, I_{Max}, are given

#259364 Received 12 Feb 2016; revised 23 Mar 2016; accepted 26 Mar 2016; published 13 Apr 2016

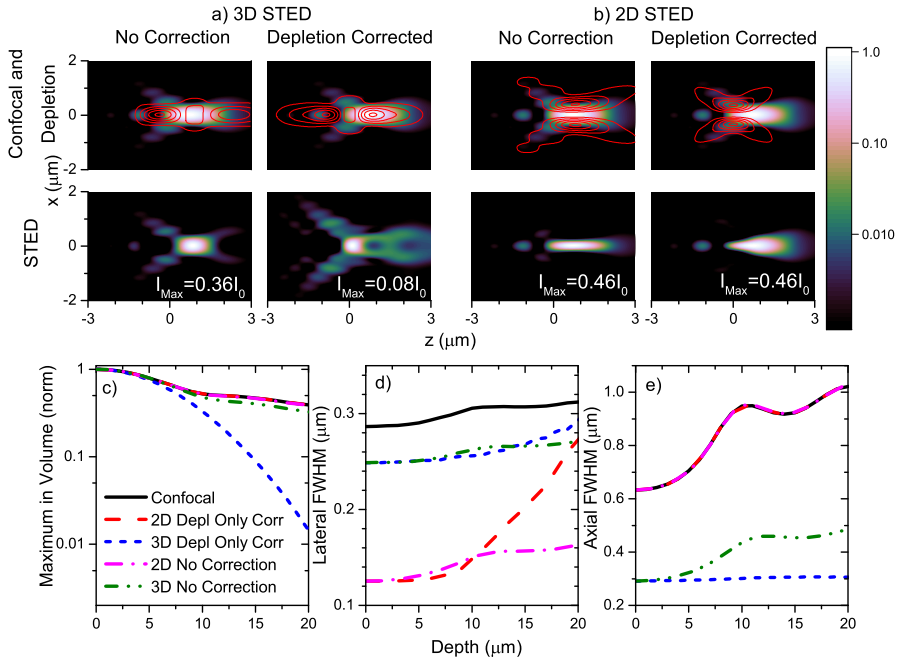

Fig. 1. The effect of correcting all three beams for an oil immersion lens imaging into glycerol. a) (b)) Calculated PSF at a depth of 15 μm . Upper row: 3D (2D) confocal (colour image) and overlaid depletion (contours at 15%, 35%, 55%, 75%, 95%) for uncorrected (left) and depletion-only corrected (right) cases. Lower row: Corresponding effective STED PSFs. Colour scale maximum, I_{Max}, given relative to unaberrated confocal maximum, I_0. c-e) Calculated plots for focal-depth dependence of confocal, 2D and 3D STED with depletion beam only correction ("Depl Only Corr") and for no correction. c) Maximum intensity throughout calculated volume (to account for focal plane shifts). d) Full-width half-maximum (FWHM) of PSF in plane parallel to focal plane at depth corresponding to maximum intensity in volume. e) FWHM through maximum along the light propagation direction.

relative to the maximum intensity in the unaberrated confocal imaging case, I_0. Despite removing the dominant defocus contribution to the spherical aberration [12, 13], the distortion of the PSF leads to a shift in the position and change in amplitude of the region of maximum intensity. In the 3D STED case the shift moves the peak into a region of stronger depletion when the STED peak is corrected; the symmetry of the zero in the 2D STED focus means that the intensity maximum, depth dependency, and axial resolution are the same as in the confocal case. However, due to the shift of the peak intensity with respect to the focal plane, the lateral resolution of 2D STED in the plane of peak intensity decreases when only the depletion beam is corrected, resulting in the apparent paradoxical effect in Fig. 1(d) of partial AO correction adversely affecting resolution. In order to better understand the depth dependence of these effects, we plot in Figs. 1(c) to 1(e) the maximum intensity and the full-width-half maximum (FWHM) of the effective STED PSF in the lateral and axial directions. These correspond respectively to the total image brightness, the lateral resolution, and the axial resolution. Despite the low refractive index mismatch, at 15 μm depth there is a significant decrease in signal intensity and resolution in all imaging modalities. Full STED performance can therefore only be achieved

#259364 Received 12 Feb 2016; revised 23 Mar 2016; accepted 26 Mar 2016; published 13 Apr 2016

if aberrations are corrected in all beam paths. This illustrates the importance of using a DM in addition to the SLM used in the depletion beam path. Any additional aberrations induced by the optical inhomogenities in the tissue will further degrade the image. While choice of 2D or 3D STED allows the effective resolution to appear high along a chosen axis of interest (e.g. in the focal plane) for an uncorrected system, it is usually accompanied by a significant decrease in the total signal and the resolution of the transverse axis. Furthermore, the modelling emphasises an important point: while other imaging techniques (such as confocal or multiphoton microscopy) can perform imaging hundreds of microns inside samples without AO, super-resolution methods will be compromised at much shallower depths. Correcting for these aberrations is the difference between obtaining an image successfully or not and the effect of increasing depth is not equivalent for all imaging techniques.

The system was implemented using the design shown in Fig. 2. A titanium sapphire laser (Spectra Physics Tsunami) provided the STED pulses and was also used to pump a supercontinuum source to generate the fluorescence excitation pulses. For the STED beam, the 80 MHz, 100 fs pulse train at 780 nm passed through a 180 mm prism of SF6 glass and was then coupled through 100 m of polarisation maintaining optical fibre in order to stretch the pulse duration to a few hundred picoseconds. At the fibre output, the collimated beam reflected off a liquid crystal SLM (Hamamatsu LCOS) which was used to generate the phase mask for the STED beam [9, 14, 15], precisely align the STED beam with the excitation beam [16] and to provide extra aberration correction to the STED beam beyond that needed for the excitation and signal paths. The SLM was imaged onto the DM (Mirao 52e) which was used as the primary aberration-correction element for all three beams. Scanning the beam in the *xy* plane of the sample was performed by a pair of galvanometer mirrors, while *z* positioning was provided by an objective lens piezo mount (Physik Instrumente Pifoc P-725) which allowed a scan range of 400 μm. The microscope objective was a 1.4 NA 100$\times$ oil immersion objective (Olympus UPLSAPO 100XO). We used a supercontinuum source (Newport SCG-02) to provide the fluorescence excitation pulses by selecting the desired excitation wavelength with an acousto-optic tuneable filter (AA Optoelectronic AOTFnC-400.650-TN) and then passed the pulses through a $\approx$2 m length of polarisation maintaining optical fibre. Coarse tuning of the STED-excitation pulse delay was performed by selecting an appropriate length of this fibre, while fine tuning was performed with a retro-reflector on a linear translation stage placed between the SF6 prism and 100 m polarisation maintaining fibre in the STED arm. The excitation pulses were combined with the STED beam at a dichroic placed between the SLM and DM.

We used two detection paths. The primary path was for imaging in confocal and STED mode and used a 50 μm core diameter fibre, corresponding to 1 Airy unit, as the detection pinhole. An avalanche photodiode collected the signal and an emission filter centred at 690 nm with a 50 nm bandpass rejected unwanted light. In order to allow imaging of the depletion focus to confirm the quality of the structured mode we also implemented a wide area (non-confocal) detection path. For this, a pellicle picked off approximately 5% of the light in the descanned path. We imaged a 40 μm diameter region of the sample onto a 500 μm core diameter optical fibre that was coupled to another avalanche photodetector.

3. Adaptive optics control scheme

3.1. Requirements for AO in STED

We use a modal, sensorless AO scheme [9] to correct for aberrations in this microscope. Specification of such a scheme requires:

1. A set of appropriate control modes for driving the AO elements
2. An image quality metric that will allow us to find the optimal aberration correction

#259364 Received 12 Feb 2016; revised 23 Mar 2016; accepted 26 Mar 2016; published 13 Apr 2016

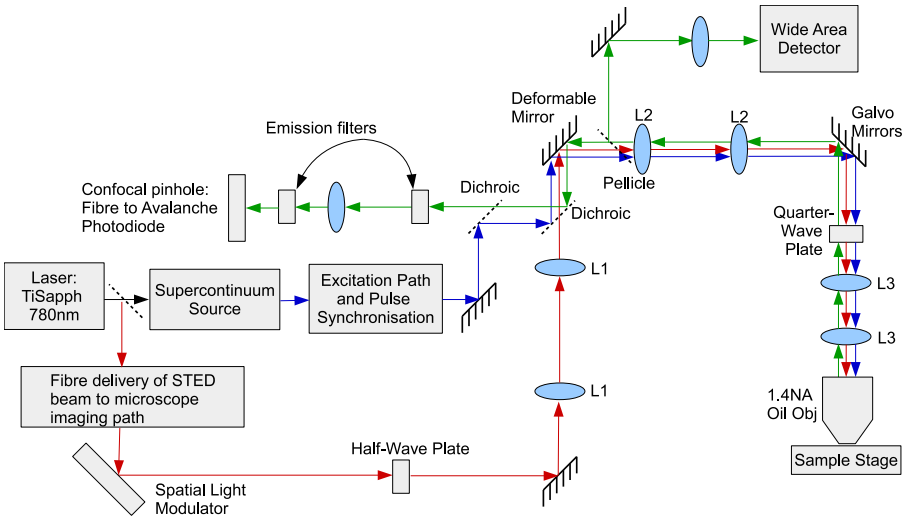

Fig. 2. Schematic of the adaptive optics STED microscope. A TiSapph oscillator provided both the STED pulses and, after passing through a supercontinuum-generating fibre, the fluorescence excitation pulses. A SLM generated the phase mask used for the structured depletion focus. The deformable mirror allowed correction of sample induced aberrations in all optical paths. A choice of detectors allowed either confocal imaging through a pinhole or wide area imaging to observe the full extent of the foci by scattering off gold beads.The SLM, DM, galvo mirrors and objective back aperture are all in conjugate planes, with the appropriate imaging performed by (non-identical) lens pairs L1, L2 and L3

3. An estimator of the metric peak, e.g. quadratic, Gaussian or Lorentzian functions

For the SLM, we model the aberrations with Zernike polynomials, which are widely used to model aberrations in optics. We follow the numbering convention used by Neil et al. [17]. Among the advantages of using Zernike polynomials are the facts that they are orthogonal, correspond to known aberration classes (such as astigmatism and coma) and allow the isolation of those modes which merely displace the focus (tip, tilt and defocus), from those which distort the focus or point spread function (PSF).

The DM consists of a deformable membrane, onto which 52 actuators are bonded in a square array. We again chose Zernike polynomials for our target control modes in order to have commonality between the two AO devices. The control modes were derived using a Shack-Hartmann wavefront sensor conjugate to the microscope objective back aperture; we illuminated a planar mirror sample with our excitation beam and used the SH sensor to estimate a decomposition of the phase function in the back aperture in terms of Zernike polynomials. The procedure for creating the Zernike control modes for the DM is fully described in [18]

The issue of the appropriate image quality metric to use for system correction is not trivial with STED imaging. When performing confocal imaging, the total image intensity is suitable and we regularly use this metric when operating the microscope in this mode. For a two-dimensional image, $I(x,y)$ the metric is defined as

$$B = \sum_{x,y} I(x,y) \tag{1}$$

Likewise, when imaging with the wide-area detection path (for example, when looking at scattered light off gold beads to measure the system PSF), we use the sum of the square of the

#259364 Received 12 Feb 2016; revised 23 Mar 2016; accepted 26 Mar 2016; published 13 Apr 2016

pixel intensities.

$$B_{Squared} = \sum_{x,y} |I(x,y)|^2 \tag{2}$$

This metric is appropriate for widefield imaging as, to a first approximation, small aberrations merely move light around the image, leading to an approximately constant image intensity. Squaring of the pixel values means that the metric preferentially responds to brighter pixels.

In the case of STED imaging, we ideally want images with constant peak brightness, corresponding to a high quality zero-intensity region in the structured PSF of the STED beam, coupled with small feature sizes, corresponding to the increased resolution allowed by the STED imaging. We have previously reported on a suitable metric [9] that combines image brightness with image sharpness:

$$M = S + \sigma\beta B\left[\frac{1}{1+e^{-k(S-S_T)}}\right] \tag{3}$$

where B and S are the brightness and sharpness (defined in terms of the second moment of the image Fourier transform) metrics respectively. We also include a logistic function that increases the contribution of the brightness metric as the image sharpness reaches a threshold S_T (typically chosen as 90% of the peak sharpness). β is a parameter that is empirically chosen to balance the contribution of B and S to the metric, while σ is either $+1$ or -1 and defines the response of the brightness to a given aberration mode. Parameter k was used to adjust the rate of transition of the logistic function in the region of $S \approx S_T$. While effective, this metric requires three empirically derived parameters which may be dependent on the sample structure. A metric with fewer empirical parameters, and which may work for STED images in a range of samples, is the Fourier Ring Correlation (FRC) metric. This was originally developed to quantify image data from electron microscopy [19] and has since been applied to superresolution microscopy images generated through single molecule switching techniques [20, 21], such as PALM and STORM. FRC uses two images, differing only in readout and shot noise, to estimate the spatial frequency at which the correlation becomes dominated by noise rather than information about the object being imaged. For two images $f_1(\vec{r})$ and $f_2(\vec{r})$, where $\vec{r}$ is the spatial coordinate, and having Fourier transforms $\widehat{f_1}(\vec{q})$ and $\widehat{f_2}(\vec{q})$ it is calculated as

$$FRC(q) = \frac{\sum_{\vec{q}\in circle} \widehat{f_1}(\vec{q})\widehat{f_2}(\vec{q})^*}{\sqrt{\sum_{\vec{q}\in circle}\left|\widehat{f_1}(\vec{q})\right|^2 \sum_{\vec{q}\in circle}\left|\widehat{f_2}(\vec{q})\right|^2}} \tag{4}$$

where we are performing the sums over pixels on the perimeters of circles of constant spatial frequency with magnitude $q = |\vec{q}|$ and where $\widehat{f_2}(\vec{q})^*$ indicates the complex conjugate of the Fourier transform of image 2. At low spatial frequencies we can see that the FRC curve as a function of q will be close to unity, while at high frequencies the (uncorrelated) noise dominates and the FRC decays to 0. Choosing an appropriate FRC threshold which defines the spatial frequency at which there is still significant signal information has been the subject of much discussion [22], particularly when considering samples which may demonstrate significant symmetry (a consideration when performing crystallographic imaging using electron microscopy). However, we have found empirically that we can use the FRC metric for aberration correction using the comparatively high threshold of 0.6. The FRC metric is also advantageous as we only need to provide a single empirical value (the threshhold) compared to the three values required for the combined metric.

Finally, in order to find the optimum correction, we used either a Gaussian or quadratic fit to the measured metric curves depending on an estimation of the degree of aberration present

#259364 Received 12 Feb 2016; revised 23 Mar 2016; accepted 26 Mar 2016; published 13 Apr 2016

in the system. With regards to getting the best quality metric curves, we have found that, in agreement with [23], for a given number of desired individual image acquisitions (e.g. when minimising photo-bleaching of the sample), we get the highest quality metric curve by reducing the number of applied amplitudes and increasing the number of image averages per amplitude. For example, if we wished to use only fifty images per mode in total, we would use five applied amplitudes with ten images averaged per amplitude rather than ten amplitudes with five averages. The increased signal to noise for each applied amplitude appears to give more robust metric curve fits.

3.2. System Alignment for AO in STED

In order to perform STED imaging on biologically relevant samples it is important first to ensure correct alignment of the system with an optically simple system. We have previously described the importance of correct phase mask alignment [10] and co-alignment of excitation and STED beams [16], while other key considerations are described in [24]. The presence of two adaptive optical elements in our system leads to additional complexity in order to obtain optimal performance. We start by ensuring that the confocal excitation and detection arms are correctly aligned. We use a sample comprised of a mix of 150 nm gold beads (BBI Solutions) and 100 nm crimson beads (Life Technologies FluoSpheres) deposited directly on a coverslip and then mounted in immersion oil. Such a sample provides a minimally aberrating specimen with which to derive a baseline correction for the aberrations intrinsic to the system due to manufacturing tolerances and residual misalignments in the microscope's components [9]. We refer to this generic correction as the instrument flat.

The first stage of generating the instrument flat is to correct the excitation and detection paths. While this is similar to aligning a conventional confocal microscope, we have noticed that the AO-STED system requires finer tolerances on the initial alignment for the best performance. One notable requirement is to have high accuracy in the coupling of the signal beam into the detection fibre. Specifically, there should be a high degree of co-alignment between the propagation axis of the beam before the fibre-focussing optics and the optical axis of the fibre. This requirement ensures that no coma is introduced by the focussing optics and that there is little coupling to higher order propagation modes in the (multi-mode) detection fibre. Having aligned the excitation and detection arms conventionally, we performed an AO correction of these paths using Zernike polynomials, typically 5 to 11, 22, and 37, on the deformable mirror, with 5 applied magnitudes of aberration per mode and, depending on the labelling density in the sample, 5 or 10 averaged frames per applied amplitude. Due to the small, but non-negligible, amount of cross-talk between modes, we found it beneficial to repeat the AO correction process two or three times. This cross-talk arises as the Zernike modes used are almost, but not perfectly optimal for sensorless correction in this microscope system. We used both the brightness (Eq. (1)) and sum of pixels squared (Eq. (2)) metrics interchangeably in the confocal path with equal success. We note that improved robustness of fit is also found by summing images obtained from a three-layer image stack with images taken at the focal plane and approximately 500 nm above and below this plane. Having optimised the excitation and detection paths we use the resulting combination of Zernike polymomials as the instrument flat on the DM.

Due to the non-common optical path taken by the STED beam before it is combined with the excitation and signal beam paths, it is to be expected that the instrument flat measured for the DM would not provide sufficient correction to allow the creation of a high quality structured focal region. An advantage of the dual AO system is that we can use the SLM to correct for those aberrations present only in the STED beam path. We follow a similar routine to that described above; we used scatter from the gold beads in the sample and detected the signal using the wide area detector. An important consideration was the choice of phase mask

#259364 Received 12 Feb 2016; revised 23 Mar 2016; accepted 26 Mar 2016; published 13 Apr 2016

for the correction routine. None of the metrics described above are effective at optimising the image of the structured focal volume generated by either the 2D or 3D STED beams and so we performed the initial correction using a plain phase mask that generated a conventional focus at the sample. As discussed previously, the STED beam is more sensitive to aberrations than the confocal beam; even after successfully correcting for the non-common path aberrations using the plain phase mask, switching to the STED masks may show some small residual focal spot distortion due to the higher sensitivity to aberrations. These are typically observed as small decenterings of the zero-intensity region or as a non-uniform azimuthal intensity profile of the surrounding high-intensity ring. Assuming correct phase mask alignment and polarisation state of the STED beam [10, 24], it is trivial to make the final required small adjustments by hand by observing the azimuthal symmetry of the intensity fluctuations and varying the appropriate Zernike modes. The RMS amplitude of these final adjustments is typically less than 0.1 radians. At this point we can also use the scatter from the gold beads to confirm the spatial overlap of the excitation and STED beams and use the tip and tilt displacement modes on the SLM to correct for any small errors [16].

3.3. Practical implementation of AO in STED

We describe here methods for aberration correction when performing STED imaging. The crimson beads on the test sample described above allow us to verify resolution enhancement from the STED system as they are amenable to depletion with the 780 nm STED beam. They also allow testing of the efficiency of different AO correction procedures. Efficient schemes are important not only because of the enhanced sensitivity to aberrations already discussed, but because the high STED laser power required for resolution enhancement may lead to bleaching or phototoxicity. In strongly aberrating media (such as deep in tissue), correction of all three optical paths using the DM is essential. However, DM based correction of the confocal signal is often not sufficient for full STED resolution enhancement and some additional SLM based correction of the STED path is required. Our preferred approach for AO with STED imaging uses both the DM and the SLM as follows:

1. Initial correction of the confocal signal using the DM
2. Rough verification of the STED correction in depletion-only mode
3. Refined aberration correction using the desired STED mask

Performing step 1 moves the system into the small aberration regime; since the correction in confocal mode can be carried out at excitation intensities that are minimally photobleaching we can apply most of the correction with the DM and in a way that minimises damage to the sample. For step 2 we take advantage of the fact that the STED depletion effect is observable at STED beam powers much lower than those required for resolution enhancement; the saturation depletion power, I_S, at which the fluorescence is decreased to 50% of the non-STED value is at least 10-20 times lower than the power typically used for STED imaging. By performing an aberration correction routine on the SLM with only the aberration correction and no STED mask applied, setting the STED power to $\approx 0.5 \times I_S$, we can look for the minimum of the metric curve (we typically use image brightness as the metric here). This improves the quality of the aberration correction on the STED arm, thereby increasing its effectiveness at depleting the signal and reducing the observed fluorescence. The required excitation and STED intensities for this step mean that photobleaching is minimal. We can then apply the desired STED phase mask and perform a correction routine on the SLM to ensure the best possible STED resolution. The choice of metric for this step is discussed in Section 3. For confirmation of the STED effectiveness with fluorescent beads, the combined metric (Eq. (3)) works well, while we have

#259364 Received 12 Feb 2016; revised 23 Mar 2016; accepted 26 Mar 2016; published 13 Apr 2016

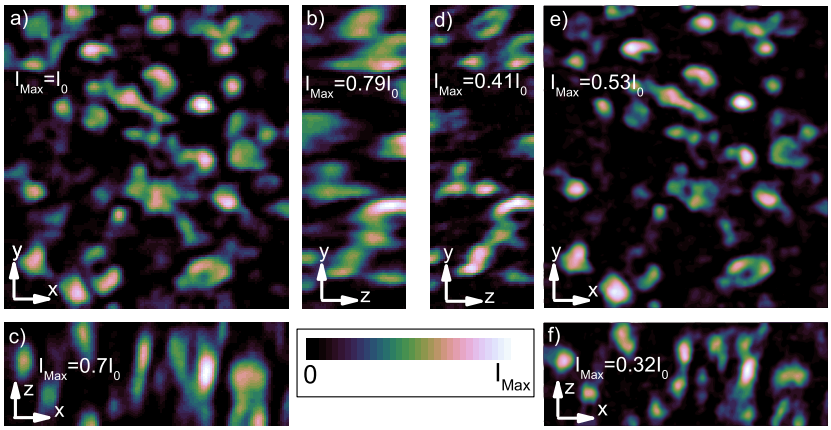

Fig. 3. Confocal and 3D STED images of Atto647N labelled vesicular glutamate transporter in synaptic boutons in intact *Drosophila* brains. Confocal sections are shown in *xy* (a), *yz* (b) and *xz* (c) planes. The imaging depth was $10\,\mu$m beneath the surface of the brain. Figures (d,e,f) show corresponding 3D STED images. The arrows indicate direction and are all $1\,\mu$m in length. The colour scale ranges from 0-I_{Max}, given as a ratio of the maximum intensity in each image, to the maximum intensity, I_0, of the confocal *xy* image.

had success with the FRC metric (Eq. (4)) with immunostained tissue samples. A particular advantage of our approach, as shown below, is that we do not need to embed sub-diffraction markers within the tissue, but can obtain super-resolution imaging by correction using the wide range of feature sizes found in biological samples.

4. Results

To demonstrate the effectiveness of the dual AO STED system in complex tissue samples we have imaged glutamatergic vesicles in neural boutons in intact brains from *Drosophila melanogaster*. To do so we incubated dissected and fixed wholemount brains with a primary antibody recognizing an epitope of the *Drosophila* vesicular glutamate transporter [25] as described in Owald et al. [26], followed by a secondary antibody coupled to Atto647N. Previous research indicates that there is probably one glutamate transporter per vesicle [27]

All the imaging results presented in this paper were processed in ImageJ by performing a $3\times$ bicubic rescaling in all axes, then performing a 3 pixel 3D median filter, followed by the subtract background function using a 300 pixel radius, with the "Sliding paraboloid" and "Disable smoothing" options enabled. We present the images using "CubeHelix" [28], a colourmap that increases linearly in perceived brightness, thereby making it suitable for colour-blind readers and reproduction in greyscale media. Figure 3 shows confocal and 3D STED images taken approximately $10\mu m$ beneath the surface of an intact *Drosophila* brain. We first performed AO correction on the confocal image using the brightness metric. The resulting images are shown in Fig. 3(a)-3(c) and show the expected morphology of the labelling within the boutons. However, due to the anisotropy of the confocal PSF, we can see structures with the expected circular cross-sections in the *xy* slices, but as these are of comparable size to the extent of the PSF in *z*, they are not clearly visible in the *xz* and *yz* slices. In order to perform 3D STED imaging, we started with the AO correction, derived during confocal imaging, on the DM and then performed an additional round of correction on the SLM using the FRC metric with a threshold of 0.6 and the correction parameters described for system alignment. The 3D STED images, Fig. 3(d)-3(f), show increased contrast, due to the STED suppressing emission from out of fo-

#259364 Received 12 Feb 2016; revised 23 Mar 2016; accepted 26 Mar 2016; published 13 Apr 2016

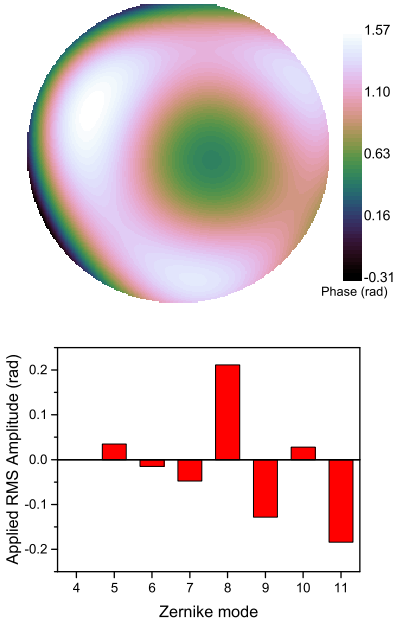

Fig. 4. Upper: The phase correction required on the deformable mirror to acquire the images in Fig. 3. This phase corresponds to an RMS wavefront error of 1.05 radians and a Strehl number of 0.33. Lower: The corresponding decomposition into Zernike polynomials. Note the strong contribution from coma (mode 8), trefoil (mode 9) and 1st order astigmatism (mode 11).

cus regions. We can also see an increase in resolution in all three dimensions. Primarily due to the increase in z resolution, it is also now possible to see the expected structures of circular cross section in all three slice directions. It is this increase in z resolution which dominates in 3D STED imaging for a given available power and, for the power available to our microscope, we see a doubling of the resolution along the optical axis when compared to the confocal case, with a correspondingly smaller increase in lateral resolution.

We can use the measured aberration coefficients to model their effects on the imaging process. Figure 4 shows the phase correction as provided by the DM for a wavelength of 780 nm, after removing the contribution from the instrument flat. The upper image is a direct reconstruction of the phase distribution as reconstructed from the applied Zernike coefficients, while the lower bar chart shows the contribution of individual modes. As expected for imaging into a medium that is mismatched in refractive index with the lens, there is a significant contribution from spherical aberration (mode 11). We also see notable amounts of coma (mode 8) and trefoil (mode 9). The extent of aberration can be quantified by the effective RMS wavefront error, σ, being corrected by the phase function. In this case $\sigma = 1.05$ rad. From this, we can also estimate the Strehl ratio as $S = e^{-\sigma^2}$, which corresponds to the ratio of the aberrated peak intensity to the unaberrated peak intensity. Strehl ratios less than 0.8 lead to poor imaging in this super-resolution microscope. The effects of the aberrations being corrected here give $S = 0.33$, implying significant aberrations in the uncorrected case. Having determined the error, we can

#259364 Received 12 Feb 2016; revised 23 Mar 2016; accepted 26 Mar 2016; published 13 Apr 2016

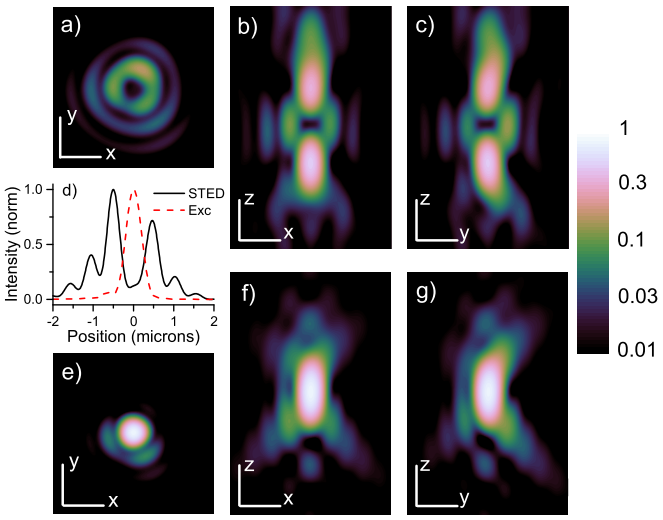

Fig. 5. a-c) Effect of the phase aberration in Fig. 4 on the 3D STED focus. d) intensity slices through the peak intensity in the focal plane x-direction for the 3D STED (solid line) and excitation (dashed line) showing both the filling in of the central zero-intensity region in the STED focus and the ≈100 nm misalignment of the excitation peak intensity with the STED minimum intensity. e-f) Effect of the phase aberration in Fig. 4 on the excitation focus. The bars are 1 μm and indicate the axes, while all colour scales are logarithmic over two orders of magnitude.

model the effects of this aberration on the PSF.

Figure 5 shows the results of modelling the foci using the procedure in [11]. Figures 5(a)-5(c) show that the 3D depletion focus is strongly aberrated; the observed distortions correspond well to the Zernike polynomials with the greatest applied coefficients. We see the effect of coma most clearly in the yz slice as it both redistributes the light in the central ring to one side and creates a curvature in the upper and lower lobes. Trefoil is most readily apparent in the xy slice, where the threefold rotational symmetry in the intensity distribution is apparent. Finally, the effect of spherical aberration is to give an uneven distribution of intensity in the upper and lower lobes. All of these effects decrease the effectiveness of the depletion beam. However, their combined effect is most apparent in Fig. 5(d), where we have taken an intensity slice along the x-axis in the focal plane. We see two effects that will adversely affect STED imaging. The first related to the width of the central low-intensity region. We have also shown a cut through the excitation focus demonstrating that it is of similar spatial extent to the low-intensity region in the STED beam. As such, in order to significantly increase the lateral spatial resolution in this case it will be necessary to have even higher laser power available than is typically used under ideal circumstances for this imaging. Secondly, and more importantly, the minimum intensity in the STED beam is 10% that of the peak intensity. This puts an absolute limit on the amount of STED power that can be used as, once the minimum power is greater than the saturation intensity, I_S, fluorescence at the centre will also be strongly depleted.

We have also calculated the focus for the excitation beam, and have shown it in Figs. 5(e)-5(f). As is expected, the observed effect on the focus is much less dramatic than for the STED beam. This is perhaps not a surprise, as (low quality) confocal images can be obtained in similar samples at depths approaching 100 μm. However, it can be seen that there *are* still effects on the focus. One notable effect occurs when looking at the combined effect of the excitation and

#259364 Received 12 Feb 2016; revised 23 Mar 2016; accepted 26 Mar 2016; published 13 Apr 2016

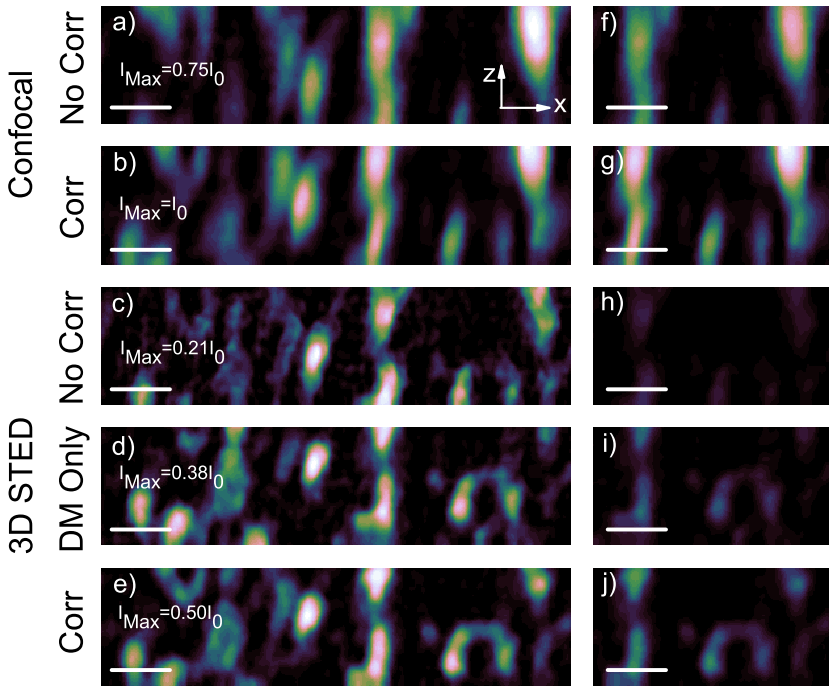

Fig. 6. The effect of dual-AO correction on STED imaging. All images are *xz* slices from the same region of a *Drosophila* brain at a depth of 15 μm. Scale bars are 1 μm. For a-e) the colour scale ranges from 0-I_{Max}, given as a scaling to the corrected maximum intensity, I_0. a) Confocal imaging with only the instrument flat applied. b) Confocal imaging after correcting for aberrations with the DM. c) 3D STED imaging with only the instrument flat applied to both the DM and SLM. d) 3D STED imaging with the correction from b) applied to the DM. e) 3D STED imaging with the correction from b) on the DM and an additional round of AO correction performed on the SLM. f-j) The right half of a-e) with constant $I_{Max}=I_0$ for all colour scales

STED foci in the line slices in Fig. 5(d). The excitation focus is shifted slightly to a positive value of x, while the minimum of the STED beam is at a negative value of x. The resulting misalignment, of order 100 nm, will also contribute to a decrease in the signal to noise in the uncorrected STED images. A similar shift between the minimum of the STED focus and the maximum of the excitation focus results in a 75 nm misalignment along the z axis.

In order to further demonstrate the effectiveness of the dual-AO correction, we present a sequence of *xz* images in Fig. 6 with varying imaging modalities and choice of aberration correction. These images were taken in a separate region of the brain to the earlier figures. The mean imaging depth was 13 μm from the surface of the brain. Figures 6(a) and 6(b) show the effect of the aberration correction, using the DM, on the confocal image. We see an increase in signal to noise ratio, contrast and a slight increase in resolution, particularly in the z-direction. Figure 6(c) shows the effect of 3D STED imaging with only the instrument flat. As we can see from Fig. 6(a), there is still confocal image information present in this case, however the extra sensitivity of the STED PSF to the aberrations mean that there is only poor imaging possible without AO correction. We see low absolute signal, higher noise and negligible increase in resolution. Futhermore, if we tried to compensate by increasing the STED power, the presence of light in the nominally zero-intensity region, as demonstrated in Fig. 5(d) would merely

#259364 Received 12 Feb 2016; revised 23 Mar 2016; accepted 26 Mar 2016; published 13 Apr 2016

lead to enhanced sample photobleaching and damage. By applying the correction to the DM that we acquired in confocal imaging mode, we recover significant STED signal, as shown in Fig.6(d). We now see better resolution increase, allowing us to discriminate features that are close to the resolution threshold in confocal microscopy. The effect is particularly noticeable in the z-direction, where the 3D STED imaging makes a significant improvement to the optical sectioning ability. Finally, by performing an iteration of AO correction on the SLM in addition to the correction present on the DM, we recovered the full potential of 3D STED imaging in this sample, as shown in Fig. 6(e).

5. Conclusion

The results presented in Fig. 3 and Fig. 6 show that aberrations can severely affect the imaging properties of 3D STED microscopes, even at modest focussing depths of around $10\,\mu$m. The major problem is the filling in of the intensity zero at the centre of the depletion beam. This filling in means that depletion of excited molecules occurs throughout the depletion focus and not just in the surrounding ring. Consequently, fewer excited fluorophores remain in the focal region and the signal level is reduced. This reduction has the further effect that the resolution is not significantly enhanced and is therefore comparable to a confocal microscope. While it is possible that in certain imaging configurations the total aberration is low, in general the aberrations will conspire to severely degrade the image quality. We have explicitly demonstrated this enhanced sensitivity to aberrations in the case of 3D STED - in aberration conditions that still allowed an acceptable image to be generated by the confocal imaging mode, we saw very poor quality imaging from the STED mode. We suspect that this requirement for extremely high quality imaging conditions to be behind the relatively low uptake of 3D STED imaging, with its application primarily constrained to imaging thin samples. We have demonstrated that these limitations can be overcome with a dual AO system - the regions of interest shown in this paper were not selected to have optimal imaging conditions, instead we merely needed to find the regions of the specimen targetted by our labelling protocol. Incorporation of AO into STED microscopes will therefore allow the use of 3D STED in thicker specimens, increasing its usefulness for biological imaging.

We have previously demonstrated adaptive optics correction of STED microscopes using either a single SLM in the STED beam or also using a second SLM in the excitation beam path [9]. Using a DM in the common path coupled with a SLM for STED phase mask generation and additional correction offers significant benefits over both conventional STED systems and our previous SLM only approach. In ensuring that all three beam paths are corrected, we can maximise contrast and signal to noise in the image. Furthermore, as shown in Fig. 5(d), different PSFs can experience relative displacements under certain aberration conditions, leading to a dynamic misalignment of the system when imaging different regions of the sample. By providing correction to all beams we correct for this error. In particular, this correction has been demonstrated based on features intrinsic to the sample and does not require the introduction of "guide-star" particles or other sub-diffraction sized references to the region of interest in the sample.

A key consideration in STED imaging is the photobleaching and phototoxicity induced by the high power required by the STED depletion beam. By improving the efficiency of the imaging process, the dual-AO STED system will maximise the effectiveness of the STED imaging. Furthermore, we have demonstrated that performing the majority of the correction required in confocal mode and using the DM allows us to take the required images for the correction in a low-photobleaching regime. As such, the overhead for the AO in terms of sample degradation is of low significance.

We have shown that the aberrations at a depth of $10\,\mu$m can be compensated by our AO

#259364 Received 12 Feb 2016; revised 23 Mar 2016; accepted 26 Mar 2016; published 13 Apr 2016

setup. Previous experiments [29] have shown that 2D STED imaging is possible at a depth of 15 μm in living mouse brains and at depths of up to 120 μm in hippocampal slices [1], both using microscope objectives with correction collars. We expect that our approach will allow imaging at equivalent depths, not only in 2D mode, which is intrinsically less sensitive to phase aberrations than the 3D mode (in particular with respect to spherical aberration), but greatly improve the isotropic optical resolution of 3D STED images at depth in tissue. The effective RMS error of 1 radian we observed at 10 μm represents less than 1% of the $\pm$50 μm stroke of our DM. As such, we can expect that imaging to a depth of 150 μm, which would encompass an entire *Drosphila* brain when mounted appropriately, will be comfortably within the DM's correction range and deeper imaging will also be possible in suitable samples.

Finally, we emphasise a key point: an acceptable STED image requires both good signal intensity and high optical resolution. Defining the quality of a STED image (or system) solely by resolution or image brightness will almost certainly allow deficiencies elsewhere to be masked.

Acknowledgments

We are grateful to Paul Scott for his assistance in sample preparation. This work was funded under Wellcome Trust grant 095927/A/11/Z. BRP was supported by a Royal Society University Research Fellowship, DO was supported by a Wellcome Trust Sir Henry Wellcome Fellowship. BRP carried out the experiments, performed the data analysis and drafted the manuscript; DB performed theoretical modelling supporting the experimental design; DO prepared samples and assisted with data acquisition; TJG assisted in experimental design and implementation; JB and MJB conceived the experimental approach, aided in data analysis and contributed to writing the manuscript. J. B. discloses significant financial interest in Bruker Corp. and Hamamatsu Photonics.

#259364 Received 12 Feb 2016; revised 23 Mar 2016; accepted 26 Mar 2016; published 13 Apr 2016